

Natural frequencies of pre-buckled rods and gridshells

Weicheng Huang^{a,b}, Longhui Qin^a, Qiang Chen^{a,b,*}

^a School of Mechanical Engineering, Southeast University, Nanjing 211189, China

^b Jiangsu Engineering Research Center of Aerospace Machinery, Southeast University, Nanjing 211189, China

ARTICLE INFO

Article history:

Received 23 October 2021

Revised 28 February 2022

Accepted 10 March 2022

Available online 18 March 2022

Keywords:

Elastic gridshells

Buckling instability

Dynamics

Numerical simulation

ABSTRACT

A discrete differential geometry (DDG)-based method is proposed to numerically study the natural frequencies of elastic rods and gridshells in their post-buckling configurations. A fully implicit numerical framework is developed based on Discrete Elastic Rods (DER) algorithm, in order to characterize the mechanical behaviors of an elastic gridshell comprised of multiple rods. When their footprints are constrained along a shrinking trajectory, the slender structures as well as their constructed network would experience a geometrically nonlinear instability and deform into an out-of-plane configuration. By checking the eigenvalues and eigenvectors of the mass and stiffness matrix, the linear vibration near the post-buckling equilibria are characterized through a numerical approach. Exploiting the efficiency and the robustness of the developed discrete method, a systematic parameter sweep is performed to quantify the vibration frequency of pre-buckled gridshells with respect to the number of rods and the pre-compressed distance. It is found that the natural frequency for both pre-deformed rods and gridshells would linearly decrease as the enlargement of compressive distance, even though the geometrically nonlinear deformations have been taken into account. Moreover, the vibration frequency almost linearly rises when the number of rods in a gridshell becomes larger. These findings could provide a fundamental insight in revealing more complex structural dynamics and facilitating the designs of buckling-induced assembly in some man-made systems, e.g., avoidance of the resonance in soft electronics.

© 2022 Elsevier Inc. All rights reserved.

1. Introduction

Thin elastic structures, such as tendrils and noodles, could perform geometrically nonlinear deformations and dramatically topological changes when subjected to common external forces or simple boundary actuations, e.g., buckling, wrinkling, folding, and snapping, which plays an important role in the design of advanced systems and intelligent metamaterials [1,2]. Also, the functionalities and potential applications can be significantly enriched if multiple slender rods are linked by joints, known as gridshells or Cosserat nets. These structures have been widely used for either aesthetic or functional purposes, such as Helsinki Zoo's Observatory Tower [3] and stretchable electronics [4,5]. Moreover, a recent trend in extreme mechanics which harnesses the buckling instabilities of slender structures to assist the designs of micro/nano engineering [6–8], bio-inspired configurations [9,10], and kirigami/origami-based patterns [11,12], indicates the need for the dynamic analysis of rod-like structures in their post-buckling regimes, where simulation-guided blueprint is necessary as it eliminates the need for painstaking trial-and-error prototyping.

* Corresponding author at: School of Mechanical Engineering, Southeast University, Nanjing 211189, China.
E-mail address: qiangchen@seu.edu.cn (Q. Chen).

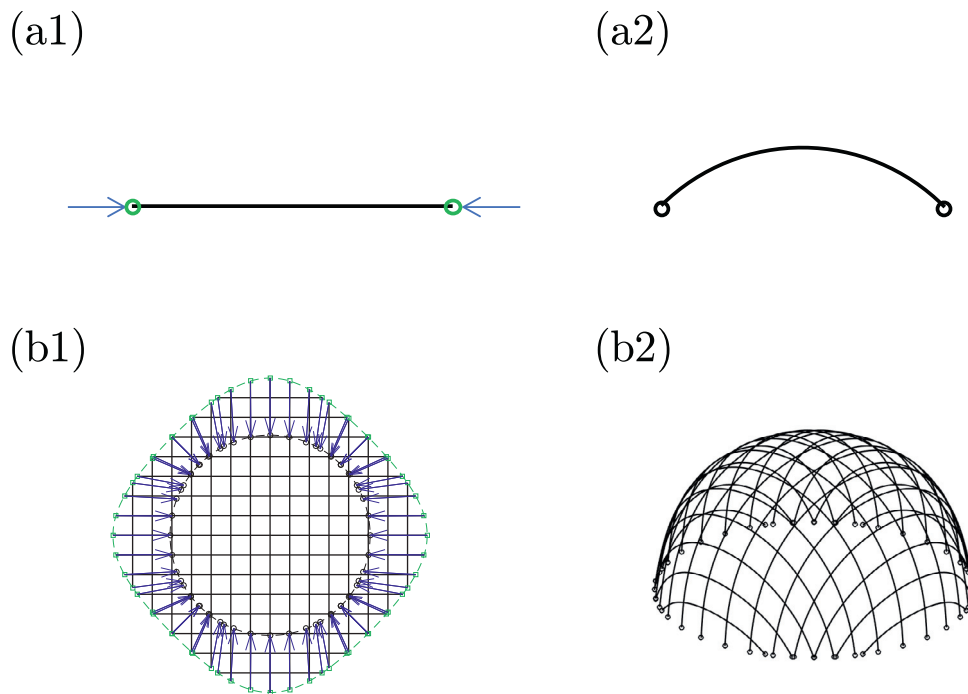


Fig. 1. Buckling instability of (a1) and (a2) an elastic rod and (b1) and (b2) an elastic gridshell with $n = 30$ rods.

The analytical solutions for a one-dimensional (1D) structure are usually derived by solving a group of ordinary differential equations (ODEs) formulated from Kirchhoff rod model [13,14]. A larger number of studies on Kirchhoff rod model could be found, e.g., Antman [15,16], Maddocks [17], Nizette and Goriely [18], and Ameline et al. [19]. Recently, the multi-stability and bifurcation of rod network are investigated through a continuous AUTO-based approach [20], in which the connection between two neighboring rods is assumed to be rigid. Instead of directly solving the ODEs with the associated initial and boundary conditions through a continuous approach, we here treat a structure as a mass-spring system and employ both space and time discretizations. The DDG-based formulations have shown powerful performances in simulating thin elastic bodies, e.g. rods [21–25], viscous threads [26], ribbons [27–29], and plates/shells [30–33]. Gridshells or Cosserat nets, however, usually behave as a two-dimensional (2D) surface consisting of multiple 1D rods, and often show different performances from both 1D slender rods and 2D thin shells. Various numerical methods were developed to realize the simulations of those special objects. Baek et al. first proposed a numerical method based on DER to investigate the form-finding problem and the rigidity measurement problem of elastic gridshells [34,35]. A stiff spring was introduced in this framework to ensure the non-deviation condition between two rods at intersecting point. Here, the joint between two contact rods was free to twist as well as rotate such that the twisting and bending coupling between two rods were not taken into account [36–40]. Nevertheless, the inverse form-finding problem – finding the initial planar shape with a given 3D target configuration – is also challenging and of general interests. Many other strategies could be found in solving this nontrivial inverse design problem, e.g., analytical formulations [34,35], data-driven methods [38,41], and physically contact-based approaches [39]. In this paper, we utilize the former form-finding strategy to construct a desired gridshell cap through buckling-induced assembly, referring to Fig. 1, and then explore the vibration behaviors near its post-buckling equilibrium.

Traditionally speaking, there are two numerical methods that are widely used for the dynamic analysis of structures – time domain method and frequency domain formulation. However, almost all numerical frameworks in DDG-based formulations employ a time domain integration to solve the discrete equations of motion step by step, for its robustness to handle the geometric nonlinearity, contact, and friction. This type of numerical integration, without doubt, is not computationally efficient when performing the linear vibration examination, especially when the target object experiences a high frequency motion, in which an infinitesimal time step size is necessary. Meanwhile, previous analyses on the dynamic vibrations [42–46] and the wave propagations [47–50] of 1D objects mainly focus on their undeformed configurations, and the geometrical nonlinearity of slender bodies is seldom considered; the vibration of mechanically-assembled 3D microstructures in their post-buckling phases is recently investigated by Refs. [51–53]. Here, motivated by the recent trend of buckling-induced assembly, the time domain method and the frequency domain formulation are combined to explore the dynamic behaviors of elastic rods and gridshells in their post-buckling phases. Specifically, the pre-buckled configuration of a thin elastic object is first derived through time domain integration and dynamic relaxation method; its dynamic performance near post-buckling

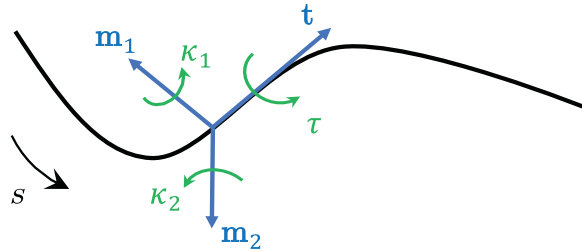


Fig. 2. Configuration of a slender rod.

equilibrium is then derived by checking the associated diagonal mass matrix and tangential stiffness matrix, while the latter one is computed based on the current geometrically nonlinear pattern. Here, the free-to-rotate joint is considered (in contrast to the rigid joint considered in Yu et al. [20]), such that an initially planar gridshell can utilize buckling instability to deform into a doubly curved shape [54], e.g., hemispherical gridshell considered in the current study. Also, to avoid the influence of artificial spring between two connected rods at joint [34,35,39–41,55], a fully implicit algorithm is developed based on DER framework and a specific mapping technique. The vibration properties of a naturally straight pin-pin beam are first explored and compared against analytical solutions. Excellent agreements between the discrete model and the analytical results demonstrate the effect of our developed DER-based framework. Moving forward, the vibration behavior of a slender rod in its post-buckling phase is discussed. A slender rod would deform into an out-of-plane configuration when compressing its boundary nodes, known as buckling instability. We find that the natural frequency of a rod in its post-buckling regime shows a linearly decreased trend as the compressive distance increased. Moreover, the m th mode of a naturally straight rod behaves similarly to the $(m - 1)$ th mode in its pre-buckled configuration. To tackle more complex scenarios of a gridshell, a fully implicit mapping algorithm is developed to simulate the mechanical response of a grid of elastic rods. The inverse form-finding process, i.e., finding the initial planar configuration from a given 3D pattern, is solved numerically by integrating the Gauss equation formulated from Chebyshev net theory [34,35]; the dynamics for both undeformed and pre-buckled gridshells are then investigated in a manner similar to the aforementioned 2D beam demonstration. The vibration frequency of a pre-deformed rod network also linearly decreases when its footprint is shrunk through a prescribed trajectory, even in a geometrically nonlinear stage. In addition, its dynamic frequency would linearly augment (even quite trivial) when the network becomes denser, which addresses the nonlocal nature of hollow grid-like structures [35].

This paper is organized as follows. In Section 2, the governing equations for 1D objects are reviewed. Then, in Section 3, the DDG-based discretization and numerical procedure for both rods and gridshells are presented in detail. Moving forward, the dynamic behaviors of pre-buckled rods and gridshells obtained from our well-established numerical frameworks are systemically discussed in Section 4. Finally, in Section 5, we present conclusive remarks and future research directions.

2. Kirchhoff rod theory

In this section, we review the classical Kirchhoff rod theory [13,14], and derive its governing equations through a variational approach. Here, we will discuss the formulations of kinematic equations, constitutive equations, and dynamic equilibrium equations.

2.1. Kinematics

Referring to Fig. 2, the structure considered here is of length L , cross-section radius r_0 (with moment of inertia $I = \pi r_0^4/4$ and cross sectional area $A = \pi r_0^2$), and is manufactured by an isotropic, linearly elastic material with Young's modulus E , Poisson's ratio ν , and density ρ . The longitudinal coordinate of structure is denoted as s , such that the 1D object can be parameterized by a space curve called centerline, $\mathbf{r}(s)$, together with a material frame, $\{\mathbf{m}_1(s), \mathbf{m}_2(s), \mathbf{t}(s)\}$, where $\mathbf{t}(s) = \mathbf{r}'(s)/|\mathbf{r}'(s)|$ is the tangential direction, and the other two directors are orthonormal to the tangent, i.e., $\mathbf{m}_1(s) \cdot \mathbf{m}_2(s) = 0$ and $\mathbf{m}_1(s) \times \mathbf{m}_2(s) = \mathbf{t}(s)$. We use $(\cdot)'$ to indicate the gradient respect to space s and $(\dot{\cdot})$ to indicate the derivative respect to time t .

The uniaxial strain of centerline is given by

$$\epsilon(s) = |\mathbf{r}'(s)| - 1, \quad (1)$$

and the rotation gradient of centerline is formulated as

$$\mathbf{m}_1'(s) = \boldsymbol{\omega}(s) \times \mathbf{m}_1(s), \quad (2a)$$

$$\mathbf{m}_2'(s) = \boldsymbol{\omega}(s) \times \mathbf{m}_2(s), \quad (2b)$$

$$\mathbf{t}'(s) = \boldsymbol{\omega}(s) \times \mathbf{t}(s), \quad (2c)$$

where $\boldsymbol{\omega}$ is the so-called Darboux vector,

$$\boldsymbol{\omega}(s) = \kappa_1(s)\mathbf{m}_1(s) + \kappa_2(s)\mathbf{m}_2(s) + \tau(s)\mathbf{t}(s). \quad (3)$$

Here, $\kappa_1(s)$ (and $\kappa_2(s)$) is the bending curvature and $\tau(s)$ is the twisting curvature. Overall, the macroscopic strains for 1D rod are the sum of elastic stretching strain in Eq. (1) and elastic curvatures in Eq. (3). However, because of the special geometry rod, e.g., $L \gg r_0$, the stretching of its centerline is more expensive than the bending and twisting, i.e., the structure is assumed to be inextensible,

$$\forall s \in (s) = 0. \quad (4)$$

2.2. Constitutive law

Based on the strains derived beforehand, we next discuss the elastic energies for a rod manufactured by an isotropic, linearly elastic material. As the object considered here is always within slender regime, the strain gradient effect is ignored and its total potential energy can be written as Audoly and Pomeau [13]

$$W_{\text{Kirchhoff}} = \int_0^L \left(\frac{1}{2}EA\epsilon^2 + \frac{1}{2}EI_1\kappa_1^2 + \frac{1}{2}EI_2\kappa_2^2 + \frac{1}{2}GJ\tau^2 \right) ds, \quad (5)$$

where $EA = E\pi r_0^2$ is the stretching stiffness, $EI_1 = EI_2 = EI = E\pi r_0^4/4$ is the bending stiffness, and $GJ = E\pi r_0^4/4(1 + \nu)$ is the twisting stiffness. Note that $EA \gg EI \sim GJ$, thus the stretching stiffness performs like a Lagrange multiplier to ensure the inextensibility of rod centerline, seeing Eq. (4).

The internal elastic force, $\mathbf{N}(s)$, and elastic moment, $\mathbf{M}(s)$, are related to the gradient of total potentials,

$$\mathbf{N}(s) = EA\epsilon(s)\mathbf{t}(s), \quad (6a)$$

$$\mathbf{M}(s) = EI_1\kappa_1(s)\mathbf{m}_1(s) + EI_2\kappa_2(s)\mathbf{m}_2(s) + GJ\tau(s)\mathbf{t}(s). \quad (6b)$$

2.3. Dynamic equilibrium equations

The dynamic equilibrium equations are the statement of force and moment balances,

$$\rho A \ddot{\mathbf{r}} = \mathbf{N}' + \mathbf{f} \quad (7a)$$

$$\dot{\mathbf{L}} = \mathbf{M}' + \mathbf{t} \times \mathbf{N}', \quad (7b)$$

where \mathbf{f} is the external force density per unit length and \mathbf{L} is the angular momentum density per unit length.

Overall, an initial boundary value problem (IBVP) is well defined and the dynamics of a slender rod can be derived by solving the differential equations and the associated initial and boundary conditions. AUTO is largely used to numerically solve the 1D IBVP through a continuous approach [56–58].

3. Discrete frameworks

In this section, we first introduce the DER algorithm [21,59] – a well-established numerical method for the geometrically nonlinear description for a single rod system; then extend it to the simulation of an elastic gridshell comprised of multiple rods. The structure here is treated as a mass-spring system and employ both space and time discretizations; the equilibrium configuration can be derived through a dynamic relaxation method. Finally, the dynamic properties near their post-buckling equilibria can be directly derived by analysing the eigenvalues and eigenvectors of the mass matrix and stiffness matrix.

3.1. Discrete elastic rods method

In the discrete setting of DER shown schematically in Fig. 3, the rod centerline is discretized into N nodes: $\mathbf{x}_0, \dots, \mathbf{x}_{N-1}$, and $N - 1$ edge vectors: $\mathbf{e}^0, \dots, \mathbf{e}^{N-2}$, such that $\mathbf{e}^i = \mathbf{x}_{i+1} - \mathbf{x}_i$, where $\mathbf{x}_i \equiv [x_i, y_i, z_i] \in \mathbb{R}^3$. Here, we use subscripts to denote quantities associated with the nodes, e.g. \mathbf{x}_i , and superscripts when associated with edges, e.g. \mathbf{e}^i . Each edge, \mathbf{e}^i , has an orthonormal adapted reference frame $\{\mathbf{d}_1^i, \mathbf{d}_2^i, \mathbf{t}^i\}$ and an orthonormal material frame $\{\mathbf{m}_1^i, \mathbf{m}_2^i, \mathbf{t}^i\}$; both of frames share the tangent as one of the directors, $\mathbf{t}^i = \mathbf{e}^i/|\mathbf{e}^i|$. The reference frame is updated at each time step through parallel transport algorithm, and, referring to Fig. 3, the material frame can be obtained from a scalar twist angle θ^i [14]. Nodal positions together with twist angles constitute the $4N - 1$ sized degrees of freedom (DOF) vector of a single rod system, $\mathbf{q} = [\mathbf{x}_0, \theta^0, \mathbf{x}_1, \dots, \mathbf{x}_{N-2}, \theta^{N-2}, \mathbf{x}_{N-1}]$.

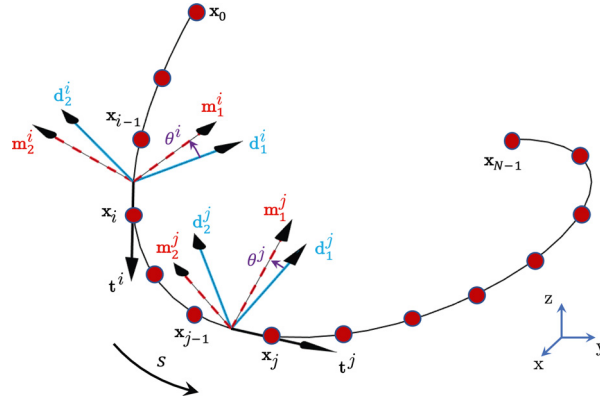


Fig. 3. Discrete diagram of a single rod system.

An elastic rod is modeled as a mass-spring system, with a lumped mass (and angular mass) at each node (and edge), and associated discrete stretching, bending, and twisting energies. The discrete elastic stretching, bending, and twisting energies are given by Bergou et al. [21, 59]

$$E_s = \frac{1}{2} \sum_{i=0}^{N-2} EA(\epsilon^i)^2 |\bar{\mathbf{e}}^i| \quad (8a)$$

$$E_b = \frac{1}{2} \sum_{i=0}^{N-1} [E_1(\kappa_{1,i} - \bar{\kappa}_{1,i})^2 + E_2(\kappa_{2,i} - \bar{\kappa}_{2,i})^2] \Delta l_i \quad (8b)$$

$$E_t = \frac{1}{2} \sum_{i=0}^{N-1} GJ(\tau_i)^2 \Delta l_i, \quad (8c)$$

where ϵ^i is the discrete stretching strain associated with the i th edge, $\kappa_{1,i}$ and $\kappa_{2,i}$ are the discrete bending curvatures at the i th node ($\bar{\kappa}_{1,i}$ and $\bar{\kappa}_{2,i}$ are the curvatures in the undeformed configuration), τ_i is the twist at the i th node, $\bar{\mathbf{e}}^i$ is the undeformed length of i th edge, and $\Delta l_i = (|\bar{\mathbf{e}}^i| + |\mathbf{e}^{i+1}|)/2$ is the Voronoi length at i th vertex. The strains, e.g., ϵ^i , $\kappa_{1,i}$, $\kappa_{2,i}$, and τ_i , can be expressed in terms of the 11 consecutive DOFs near i th node, $\{\mathbf{x}_{i-1}, \theta^{i-1}, \mathbf{x}_i, \theta^i, \mathbf{x}_{i+1}\}$,

$$\epsilon^i = \frac{|\mathbf{e}^i|}{|\bar{\mathbf{e}}^i|} - 1, \quad (9a)$$

$$\kappa_{1,i} = \frac{\mathbf{e}^{i-1} \times \mathbf{e}^i}{|\mathbf{e}^{i-1}| |\mathbf{e}^i| + \mathbf{e}^{i-1} \cdot \mathbf{e}^i} \cdot \frac{(\mathbf{m}_2^{i-1} + \mathbf{m}_2^i)}{\Delta l_i} \quad (9b)$$

$$\kappa_{2,i} = -\frac{\mathbf{e}^{i-1} \times \mathbf{e}^i}{|\mathbf{e}^{i-1}| |\mathbf{e}^i| + \mathbf{e}^{i-1} \cdot \mathbf{e}^i} \cdot \frac{(\mathbf{m}_1^{i-1} + \mathbf{m}_1^i)}{\Delta l_i} \quad (9c)$$

$$\tau_i = \frac{(\theta^i - \theta^{i-1} + m_i^{\text{ref}})}{\Delta l_i}, \quad (9d)$$

where m_i^{ref} is the reference twist associated with the reference frame [14,21,59]. Finally, the elastic forces (associated with nodal positions) and elastic moments (associated with the twist angles) are the negative gradient of total potentials,

$$\mathbf{F}^{\text{int}} = -\frac{\partial}{\partial \mathbf{q}} (E_s + E_b + E_t), \quad (10)$$

and the tangential stiff matrix (also known as Hessian matrix) is the second variation of total potentials,

$$\mathbb{K} = -\frac{\partial \mathbf{F}^{\text{int}}}{\partial \mathbf{q}} \equiv \frac{\partial^2}{\partial \mathbf{q}^2} (E_s + E_b + E_t). \quad (11)$$

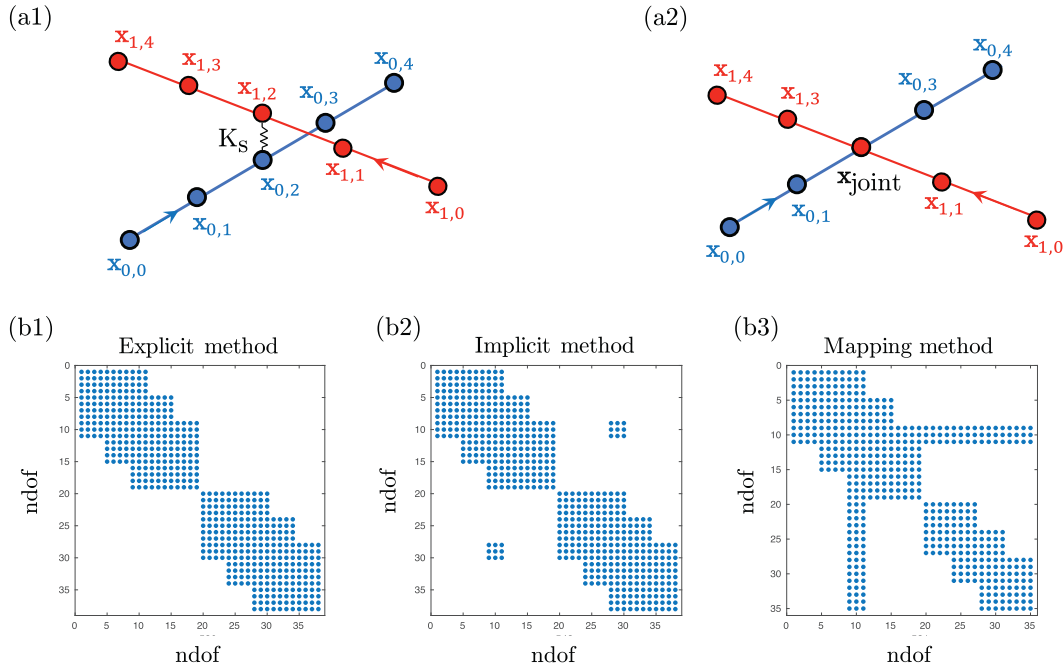


Fig. 4. (a1) and (a2) Schematic diagrams of a gridshell comprised of two rods. (a1) Two rods connected by a stiff spring. (a2) Two rods connected by a joint point. (b1)–(b3) Tangential stiffness matrix of three different methods: (b1) explicit method; (b2) implicit method; and (b3) mapping method.

3.2. Discrete elastic gridshells method

Now we derive the discrete simulation for an elastic gridshell consisted of multiple rods. A new DOF vector, $\hat{\mathbf{q}}$, that contains all DOFs of a gridshell with n rods is constructed as follow,

$$\hat{\mathbf{q}} = [\mathbf{q}_0, \mathbf{q}_1, \dots, \mathbf{q}_r, \dots, \mathbf{q}_n], \quad (12)$$

where \mathbf{q}_r is the DOF vector of the r th rod, and the size of which is $4N_r - 1$ (N_r is node number of r th rod).

Only DER model is insufficient to simulate elastic gridshells if the joint between two rods at the intersected area is ignored. In Fig. 4(a1), two nodes, $\mathbf{x}_{0,2}$ and $\mathbf{x}_{1,2}$, from two different rods overlap at the joint. Here, the position of the j th node on i th rod within a gridshell system is denoted as $\mathbf{x}_{i,j}$. A straightforward method to enforce the coincidence of two nodes at the joint is a linear spring-like energy of the form

$$E_c = \frac{1}{2} K_s |\mathbf{x}_{0,2} - \mathbf{x}_{1,2}|^2, \quad (13)$$

where K_s is the Lagrange multiplier. Its negative gradient, $-\partial E_c / \partial \hat{\mathbf{q}}$, is included as an elastic force in a gridshell system. The Hessian matrix of this system can be trivially computed to aid the Newton's method in the solution of equations of motion. There are two ways to solve the linear system comprised of several rods connected by stiff springs: (i) *Explicit method*. In this case, we only consider the diagonal terms in the stiffness matrix formulated in Eq. (13), e.g., $\{\partial^2 E_c / \partial \mathbf{x}_{0,2}^2, \partial^2 E_c / \partial \mathbf{x}_{1,2}^2\}$, while the off-diagonal elements, $\{\partial^2 E_c / \partial \mathbf{x}_{0,2} \partial \mathbf{x}_{1,2}, \partial^2 E_c / \partial \mathbf{x}_{1,2} \partial \mathbf{x}_{0,2}\}$, are ignored. This method shows good performance when the stiffness K_s is suitably chosen; however, if the spring stiffness is too small, there will be a deviation between two rods at the intersecting point; on the other hand, if the spring stiffness is too large, the convergence of our simulator would be poor. The benefit of this approach is that its Hessian matrix reminds banded, referring to Fig. 4(b1), such that its time complexity is $O(N)$ [60]. Due to its straightforward implementation and computational efficiency, this type of method is largely used for the simulation of elastic gridshells [34,35,40,41]. (ii) *Implicit method*. In contrast to the previous scenario, implicit method considers both diagonal and off-diagonal components, e.g., $\{\partial^2 E_c / \partial \mathbf{x}_{0,2}^2, \partial^2 E_c / \partial \mathbf{x}_{0,2} \partial \mathbf{x}_{1,2}, \partial^2 E_c / \partial \mathbf{x}_{1,2} \partial \mathbf{x}_{0,2}, \partial^2 E_c / \partial \mathbf{x}_{1,2}^2\}$. The shape of corresponding Hessian matrix is illustrated in Fig. 4(b2). This implicit framework shows better convergence compared with the previous explicit approach; however, the Hessian matrix here is no longer diagonal, such that we cannot make full use of the banded matrix solver, which is computationally efficient. Both implicit and explicit methods could give a reasonable prediction when studying the quasi-static response of an elastic gridshell, e.g., form finding problem in elastic gridshells [34,35,40,41], because the Hessian matrix used in Newton-Raphson method only influence the convergent speed, while has no contribution to the final equilibrium results.

On the other hand, to avoid the influence of artificial spring, a *mapping method* is proposed. Here, rather than treating the two nodes at the contact area separately, a single node is used to represent the crossing point. As shown in Fig. 4(a2),

$\mathbf{x}_{\text{joint}}$ is on two separate rods, and a new DOF vector is assembled through a specific mapping,

$$\tilde{\mathbf{q}} = \mathbb{T}(\hat{\mathbf{q}}). \quad (14)$$

Note that $\tilde{\mathbf{q}} \equiv \hat{\mathbf{q}}$ for both *explicit method* and *implicit method*. With this mapping technique, the spring is no longer necessary and the choice of spring stiffness K_s is naturally resolved. Moreover, the size of DOF vector is reduced by $T \times 3$, where T is the number of crossing points. Fig. 4(b3) shows the pattern of Hessian matrix in *mapping method*. The internal force vector, $\tilde{\mathbf{f}}^{\text{int}}$, and the associated tangential stiffness matrix, $\tilde{\mathbb{K}}$, can also be made up by transforming all the quantities of individual rod system to a global gridshell framework through the proposed mapping algorithm, \mathbb{T} . The issues of explicit method and implicit method are detailed in [Appendix A](#).

3.3. Structural dynamics

The equations of motion for both rod and gridshell systems are

$$\tilde{\mathbb{M}}\ddot{\tilde{\mathbf{q}}} = \tilde{\mathbf{f}}^{\text{int}} + \tilde{\mathbf{f}}^{\text{ext}}, \quad (15)$$

where $\tilde{\mathbf{f}}^{\text{ext}}$ is the external force vector (e.g. gravity and damping force), and $\tilde{\mathbb{M}}$ is the diagonal mass matrix comprised of the lumped masses. Newmark-beta method is used to update the DOF vector $\tilde{\mathbf{q}}$ and its velocity (time derivative of DOF) $\tilde{\mathbf{v}} = \dot{\tilde{\mathbf{q}}}$ from time step t_k to $t_{k+1} = t_k + h$ (h is the time step size):

$$\tilde{\mathbb{M}}\Delta\tilde{\mathbf{q}}_{k+1} - h\tilde{\mathbb{M}}\tilde{\mathbf{v}}_k - h^2\beta^2(\tilde{\mathbf{f}}_{k+1}^{\text{int}} + \tilde{\mathbf{f}}_{k+1}^{\text{ext}}) - h^2\beta(1-\beta)(\tilde{\mathbf{f}}_k^{\text{int}} + \tilde{\mathbf{f}}_k^{\text{ext}}) = \mathbf{0} \quad (16a)$$

$$\tilde{\mathbf{q}}_{k+1} = \tilde{\mathbf{q}}_k + \Delta\tilde{\mathbf{q}}_{k+1} \quad (16b)$$

$$\tilde{\mathbf{v}}_{k+1} = \frac{1}{h\beta}\Delta\tilde{\mathbf{q}}_{k+1} - \frac{1-\beta}{\beta}\tilde{\mathbf{v}}_k, \quad (16c)$$

where superscript $k+1$ (and k) denotes evaluation of the quantity at time t_{k+1} (and t_k), and β is a parameter between 0.5 and 1.0. The Jacobian associated with [Eq. \(16\)](#) required for Newton's iteration is

$$\tilde{\mathbb{J}} = \tilde{\mathbb{M}} + h^2\beta^2\tilde{\mathbb{K}}, \quad (17)$$

where the tangential stiffness matrix $\tilde{\mathbb{K}}$ are evaluated at $t = t_{k+1}$. The gradient of the external force vector, $\partial\tilde{\mathbf{f}}^{\text{ext}}/\partial\tilde{\mathbf{q}}$, is ignored, i.e., external forces are treated explicitly.

Time domain analysis is an effective way when performing the geometrically nonlinear dynamics of slender structures; however, it would experience a painstaking trail during the vibration investigations, especially for the high frequency case, in which the time step size h used in Newmark-beta scheme has to be small enough to avoid numerical issues. The frequency domain analysis, on the other side, could directly provide the natural frequency and its corresponding mode shape when pre-buckled structure undergoing a linear vibration around its equilibrium configuration,

$$(\tilde{\mathbb{K}} - \omega_m^2\tilde{\mathbb{M}})\delta\tilde{\mathbf{q}}_m = \mathbf{0}, \quad (18)$$

where ω_m is the m th natural frequency of a dynamic system and $\delta\tilde{\mathbf{q}}_m$ is its associated vibration mode shape. MATLAB is used to check the eigenvalues and the eigenvectors of diagonal mass matrix, $\tilde{\mathbb{M}}$, and tangential stiffness matrix, $\tilde{\mathbb{K}}$. Specifically, the tangential stiffness matrix is formulated when the elastic object undergoes a geometrically nonlinear instability.

4. Results

In this section, the dynamic performances of an elastic rod and its network will be presented. We first study the vibration performance of a naturally straight pin-pin beam, for the comparison with analytical solution; the dynamic behavior of a pre-buckled pin-pin beam is later investigated. Finally, we turn our focus to the dynamics of a gridshell comprised of multiple rods connected through joints.

4.1. Dynamics of a straight pin-pin beam

We will get start with the simplest case: a naturally straight pin-pin beam, to compare with analytical solution, which is provided in [Appendix B](#).

The physical parameters are: rod length $L = 1.0$ m, cross-section radius $r_0 = 1.0$ cm, Young's modulus $E = 1.0$ GPa, shear modulus $G = E/3$ (i.e., incompressible material with Poisson's ratio $\nu = 0.5$), density $\rho = 1000.0$ kg/m³. For a single rod system, its DOF vector is straightforward, $\tilde{\mathbf{q}} \equiv \hat{\mathbf{q}} \equiv \mathbf{q}_0$. The number of vertex is set to be $N = 100$ after a convergent study. All z positions, z_i (with $i \in [0, N-1]$), as well as twisting angles, θ^i (with $i \in [0, N-2]$), are constrained to ensure the planar motion of a rod. The first and last nodes, $\{\mathbf{x}_0, \mathbf{x}_{N-1}\}$, are also fixed to guarantee the pin-pin boundary condition. All other nodes are free to evolve based on the statement of force balance. The natural frequency is derived by checking the eigenvalues and the eigenvectors of [Eq. \(18\)](#). [Fig. 5](#) shows the first 6 vibration modes of a naturally straight pin-pin beam from

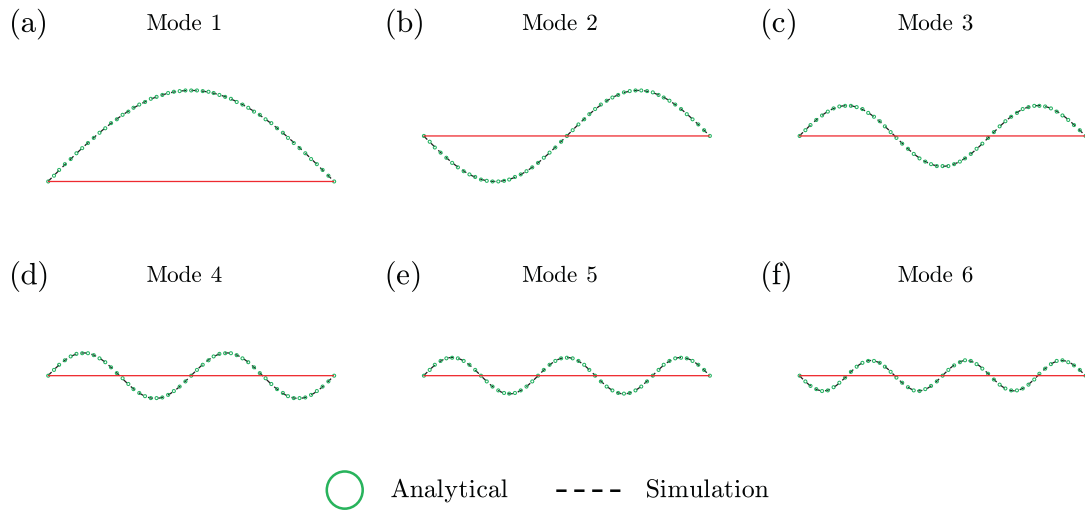


Fig. 5. Dynamic modes of a pin-pin beam.

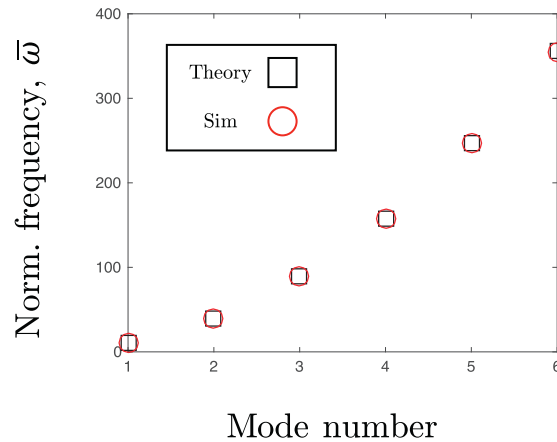


Fig. 6. Normalized frequency as a function of mode number for a pin-pin beam.

Table 1
Normalized natural frequencies for a pin-pin beam.

Method	Numerical solution	Analytical solution
Mode 1	9.8688	9.8696
Mode 2	39.4652	39.4784
Mode 3	88.7594	88.8264
Mode 4	157.7018	157.9137
Mode 5	246.2229	246.7401
Mode 6	354.2337	355.3058

both analytical solutions (which are derived in Eq. (B.3)) and numerical predictions, and Fig. 6 (as well as Table 1) provides the relation between the natural frequency and the mode number. Here, the natural frequency is normalized as follow,

$$\bar{\omega} = \omega L^2 \sqrt{\frac{\rho A}{EI}}. \quad (19)$$

Quantitative agreement between numerical simulation and analytical solution indicates the accuracy of our DDG-based model when performing the dynamic behaviors of slender structures.

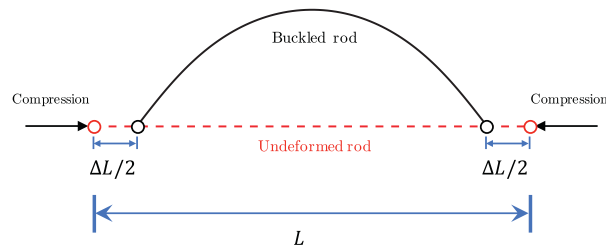


Fig. 7. Numerical setup for a pre-buckled planar rod.

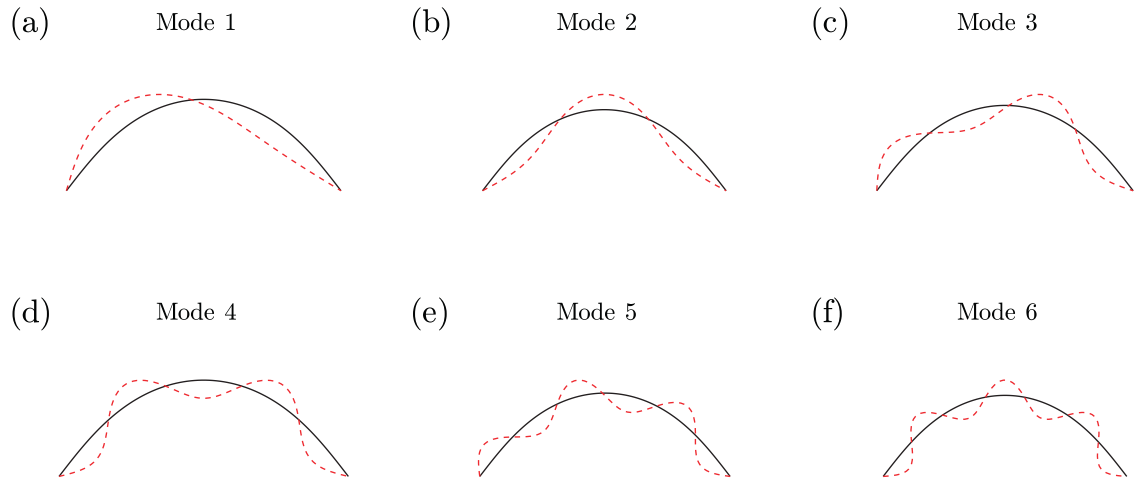


Fig. 8. Dynamic modes of a pre-buckled planar rod.

4.2. Dynamics of a pre-compressed pin-pin beam

Next, the dynamic property of a planar pin-pin rod in its post-buckling regime will be discussed in detail. The slender rod would experience buckling instability when the uniaxial compressive load is beyond a threshold; this problem has been studied since the days of the elastica theory of Euler in the 18th century. As the object is modeled as an inextensible rod, the threshold compressive displacement that inducing the instability of structure is assumed to be zero, i.e., we mainly focus on its post-buckling regime.

The physical parameters and boundary conditions used in this case are identical to the previous naturally straight beam; the uniaxial pre-compressed distance is denoted as ΔL , referring to Fig. 7. Fig. 8 illustrates the dynamic modes of a pre-buckled planar rod with a pin-pin boundary condition; here, the pre-compressed distance is set to be $\Delta L/L = 0.2$. Next, in Fig. 9, we plot the variation of normalized natural frequency, $\bar{\omega}$, on normalized pre-compressed displacement, $\Delta L/L$. The natural vibration frequency linearly decreases as the increasing of uniaxial compression in structural post-buckling regime, even when the geometrically nonlinear deformation is taken into account. Interestingly, the dynamic mode and its related vibration frequency of a pre-buckled rod show quantitative agreements with the lower mode in its naturally straight pattern, referring to Figs. 8(a) and 5(b), i.e., in Fig. 9, the extension line of m th mode of a pre-buckled rod would pass through the $(m - 1)$ th mode of an undeformed rod. Because the configuration of a pre-buckled rod is similar to the first vibration mode of a straight beam, it could only vibrate starting from a higher frequency and higher mode. As both buckling instability and dynamic vibration are eigenvalues and eigenvalues problems, when the beam is in its post-buckling regime, its first dynamic frequency would be negative and meaningless, such that it could only start from the second mode. Details are in Appendix C.

4.3. Dynamics of an elastic gridshell

Moving forward, we will pay our attention to the main contribution of the current study and investigate a more complex system comprised of multiple thin rods. We first review the buckling-induced assembly and the shape construction of a gridshell cap [34,35,39–41], and next study the dynamic behaviors of both undeformed and pre-buckled elastic gridshells.

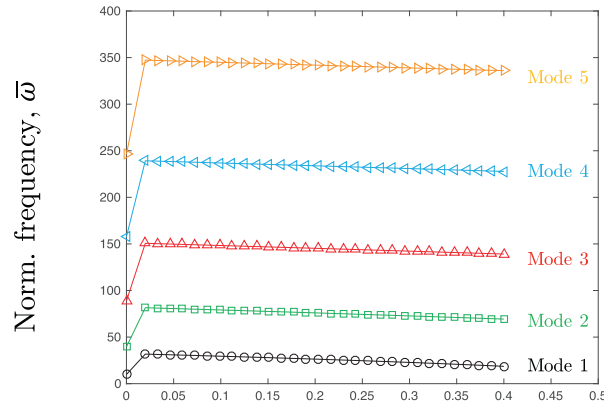


Fig. 9. Normalized frequency as a function of pre-compressed distance for a pre-buckled beam with pin-pin boundary condition.

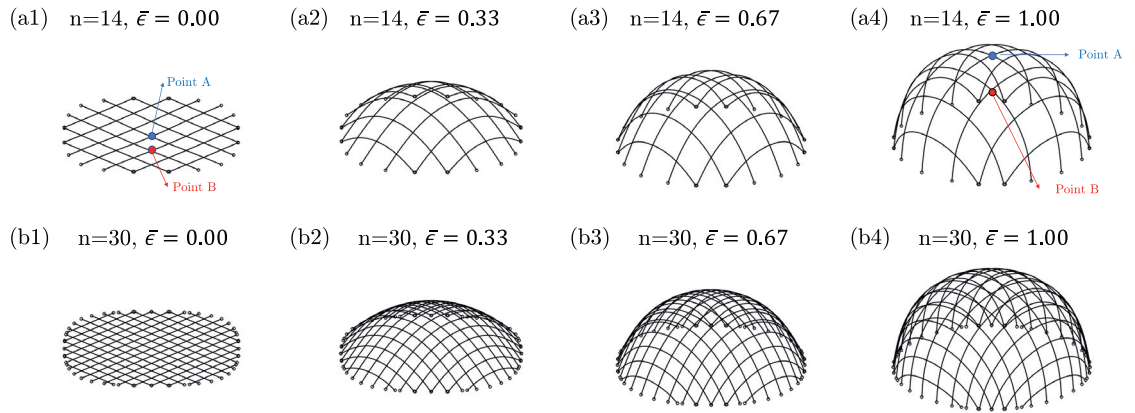


Fig. 10. Shape construction process of pre-stressed hemispherical gridshells. (a1)–(a4) Rod number $n = 14$. (b1)–(b4) Rod number $n = 30$.

The presented numerical framework can predict the mechanical responses of an elastic gridshell under arbitrary boundary and loading conditions, while the inverse process, i.e., finding the initial planar configuration from a given 3D pattern, is also challenging. Chebyshev net theory was adopted to find the initially planar pattern of a gridshell and its corresponding trajectories on footprints [34,35]. Overall, a hemispherical gridshell cap can be constructed with a prescribed planar shape and a specific trajectory applied on its extremities. Details of form finding process for elastic gridshells can be found in the Supporting Information Appendix of Ref. [34]. The contact-based form finding method and the data-based form finding procedure are presented in Refs. [40,41], separately.

The material parameters are identical to the previous planar rod scenario: Young's modulus $E = 1$ GPa, shear modulus $G = E/3$, material density $\rho = 1000.0$ kg/m³. The length of two longest rods in a planar gridshell is chosen to be $L = 1.00$ m for consistency. The discrete edge length is set to be $\Delta l = 1$ cm. Convergent study is provided in Appendix D. The boundary nodes, $\{\mathbf{x}_{r,0}, \mathbf{x}_{r,N_r-1}\}$, as well as the boundary angles, $\{\theta^{r,0}, \theta^{r,N_r-2}\}$, for all rods (with $r \in [0, 1, 2, \dots, n-1]$) are constrained to achieve the pin-pin boundary conditions. To construct a hemispherical cap from a planar grid of rods by utilizing buckling instability, a specific 2D configuration has been chosen, referring to Fig. 10(a1) and (b1). The shape construction process is derived through a time domain integration, i.e., the boundary nodes are manually moved along a prescribed path with an extremely low speed, $v_{bc} = 1$ mm/s, in order to avoid inertial effect and higher order dynamic buckling modes; the boundary angles, similarly, are fixed as zeros all the time to avoid rigid body rotations. Here, $\bar{\epsilon} = \Delta L / \Delta L_{\max}$ is used to evaluate the compressive level of a pre-buckled gridshell cap, where ΔL_{\max} is the compressive distance for a perfect hemispherical gridshell. Fig. 10 illustrates some representative gridshell caps in their post-buckling regimes, e.g., with $\bar{\epsilon} \in \{0.00, 0.33, 0.67, 1.00\}$ and $n \in [14, 30]$. With the novel mapping-based numerical framework and hemispherical gridshell cap constructed beforehand, the dynamic behaviors of a gridshell near any given equilibrium configurations can be easily derived by examining the local tangential stiffness matrix, $\hat{\mathbb{K}}$, and the local diagonal mass matrix, $\hat{\mathbb{M}}$.

We first consider the dynamics of a planar grid of rods, $\bar{\epsilon} = 0.00$. Fig. 11 (as well as Supplementary Material) illustrates first 5 dynamic modes of a planar gridshell comprised of $n = 14$ and $n = 30$ rods. Here, the mode 2 and the mode 3 are

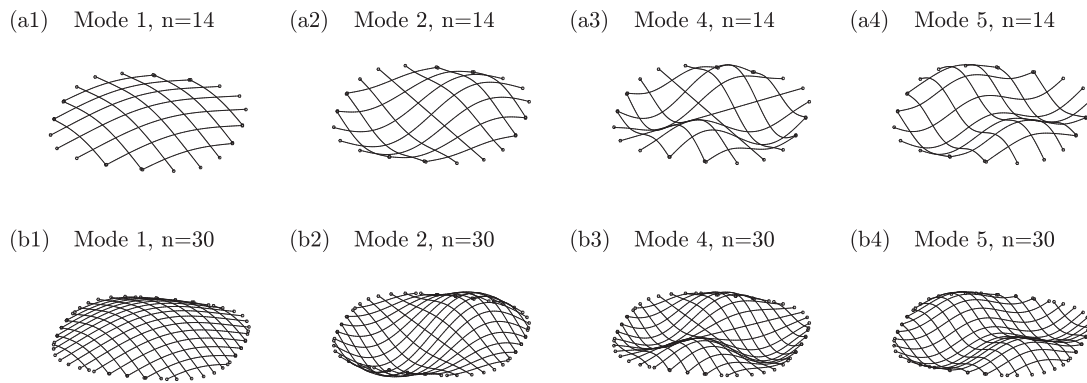


Fig. 11. Dynamic modes of an undeformed gridshell consisted of (a1)–(a4) $n = 14$ rods and (b1)–(b4) $n = 30$. Here, the structural displacements are rendered by exaggeration. Here, the 3rd mode is the rotation of 2nd mode. The corresponding videos can be found in Supplementary Material.

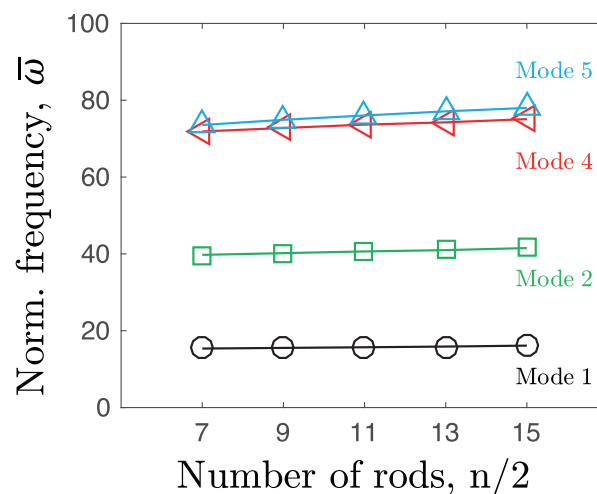


Fig. 12. Normalized frequency as a function of rod density in an undeformed gridshell. Here, the 3rd frequency is identical to the 2nd frequency.

symmetric to each other, and, therefore, their natural frequencies are identical; mode 4 and mode 5, interestingly, are similar to each other but not totally symmetric, i.e., the longest rods in mode 4 are straight lines, which differs from the behavior observed in mode 5. Also, as expected, the vibration frequency of mode 5 is slightly higher than the one in mode 4, referring to Fig. 12. The natural frequency of planar gridshell is linearly related to its rod density, n , even quite trivial.

Then, in Fig. 13, we provide some snapshots for the dynamic modes of a pre-buckled hemispherical gridshell (with pre-compressed distance $\bar{\epsilon} = 1.00$ and number of rods $n = 14$ and $n = 30$). The associated dynamic renderings can be found in Supplementary Material. Here, the first 5 dynamic modes are analysed: the first vibration mode is along the angle bisections between x axis and y axis; the second mode, on the other hand, presents a triangle-like pattern; next, the third mode is symmetric to the previous case – just by rotating mode 2 through a certain angle, and the frequency of these two are identical; in contrast to the previous bending-dominated patterns, mode 4 performs like a twisting-dominated vibration. Details can be found in Supplementary Material. Finally, mode 5 is extension of mode 2 (and 3), i.e., its configuration increases from a triangle-like configuration to a square-like profile. A similar tendency can be found for gridshells comprised of different numbers of rods, n , and undergoing different compressive distance, $\bar{\epsilon}$. Fig. 14 presents the relations between the normalized frequency, $\bar{\omega}$, and the normalized compressive distance, $\bar{\epsilon}$, for different numbers of rods, $n \in \{14, 22, 30\}$. As expected, the vibration frequency almost linearly decreases as the enlarge of the pre-buckled level, in a manner similar to the previous pin-pin beam. On the other side, Fig. 15 shows the dependence of natural frequency on number of rods in an elastic gridshell, with different pre-compressed distance, $\bar{\epsilon} \in \{0.2, 0.4, 0.8\}$. As the structure becomes denser, the magnitude of its natural frequency also performs a linear-like incremental trend, which shows similarity to the rigidity measurements and the asymptotic behaviors of elastic gridshells presented in Ref. [35]. We do not find any governing law for the dynamic behaviors between a planar gridshell and its deformed configuration at this stage. The time domain analysis for mode 1 is obtained for the comparison with frequency domain analysis, referring to Appendix E.

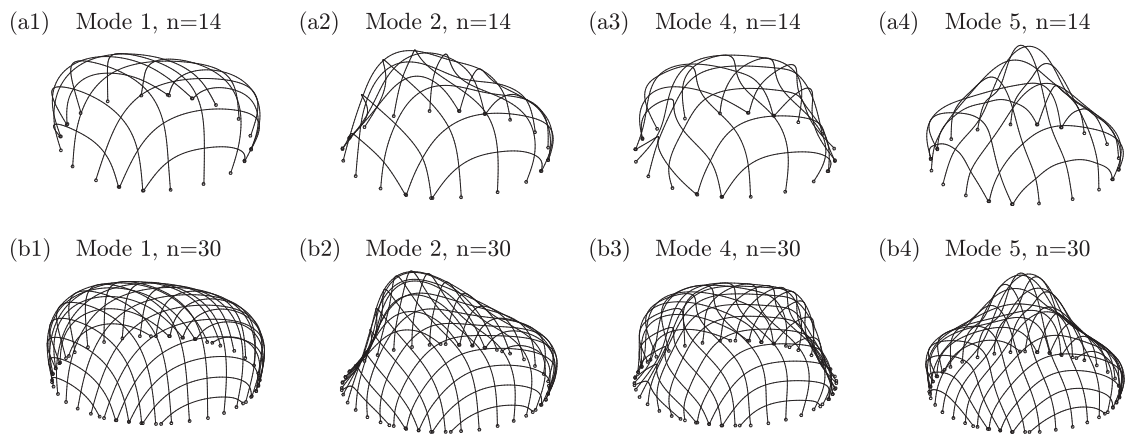


Fig. 13. Dynamic modes of a pre-buckled hemispherical gridshell (with $\bar{\epsilon} = 1.00$) comprised of (a1)–(a4) $n = 14$ rods and (b1)–(b4) $n = 30$. Here, the structural displacements are rendered by exaggeration. The corresponding videos can be found in Supplementary Material.

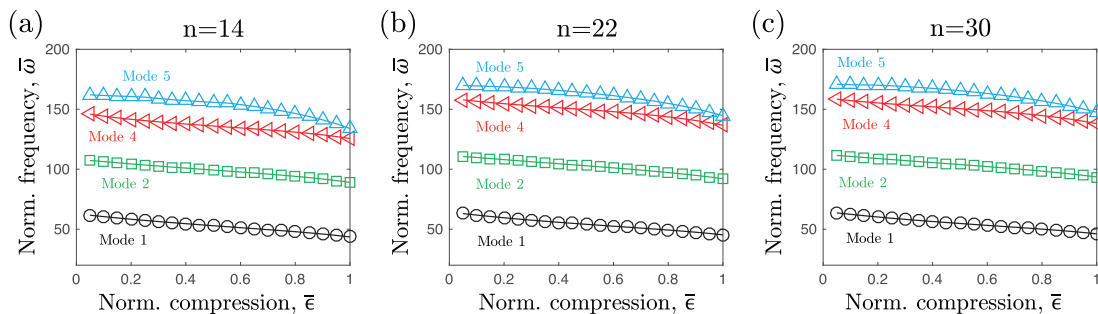


Fig. 14. Relations between the normalized frequency, $\bar{\omega}$, and normalized compression, $\bar{\epsilon}$, for gridshells comprised of different numbers of rods: (a) $n = 14$; (b) $n = 22$; and (c) $n = 30$.

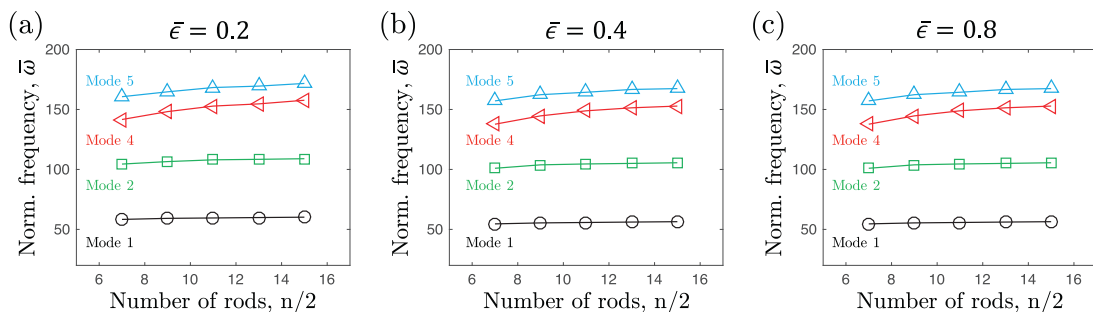


Fig. 15. Normalized frequency, $\bar{\omega}$, as a function of rod number, n , for different compressive distance: (a) $\bar{\epsilon} = 0.2$; (b) $\bar{\epsilon} = 0.4$; and (c) $\bar{\epsilon} = 0.8$.

5. Conclusion

In this paper, we have numerically examined the natural frequencies of a pre-buckled rod and its network with a pin-pin boundary condition. For this purpose, a DER-based mapping algorithm has been introduced to study the mechanical response of a grid of rods connected through rigid joints. A single rod would undergo buckling instability when the compressive load beyond a threshold, known as Euler's Elastica; next, its dynamic properties near the post-buckling equilibrium has been derived by checking its diagonal mass matrix and local stiffness matrix, which was calculated within a geometrically nonlinear deformation. The natural frequency of a pre-buckled rod linearly decreased as the enlarge of uniaxial compression; also, the m th mode of a rod in its post-buckling regime shown similarity to the $(m + 1)$ th mode in its stress-free configuration. For a system comprised of multiple rods, the inverse design procedure was first evaluated based on Chebyshev nets theory. Then, its dynamic behavior has been fully investigated in a manner way similar to the previous planar

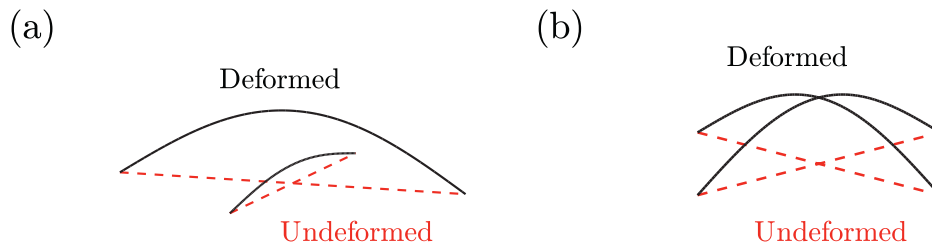


Fig. A1. The eigen mode derived from (a) explicit method (as well as implicit method) with $K_s = 10^2 EI$ and (b) mapping method.

beam scenario. The natural frequency of a pre-buckled gridshell also performs a linear decline when shrinking its boundary footprints along a prescribed path. Moreover, the vibration frequency almost linearly rises when the number of rods in a gridshell becomes denser.

Here, we mainly limited ourselves to a coarse structure – the distance between two neighboring rods is much larger than their radius. The dynamics of a finer net would be of interest for future investigation, e.g., finding a more general theory to describe the nonlinear dynamics of continued shells, knitted sweaters, and hollow nets. In closing, we hope our proposed discrete framework and its corresponding numerical results can motivate some innovative designs in both civil and mechanical engineered structures, e.g., avoid resonance in architectures or soft electronics.

Acknowledgments

This work was supported by the [Fundamental Research Funds for the Central Universities](#) (No. 2242021R10024) and the [Jiangsu Planned Projects for Postdoctoral Research Funds](#) (2021K230B).

Appendix A. Issues in explicit method and implicit method

In this appendix, we discuss the numerical issues in explicit method and implicit method. Here, a simple structure comprised of two connected rods is considered. Referring to [Fig. A.16\(a\)](#), deviation between connected area is observed when the K_s formulated in [Eq. \(13\)](#) is small (e.g., $K_s = 10^2 EI$), for both explicit method and implicit method; mapping method, on the other side, can solve this issue automatically, seeing [Fig. A.16\(b\)](#) for details. Moreover, the tangential stiffness matrix may not be symmetric positive definite and the numerical issue would appear if K_s is extremely large, for both implicit method and explicit method, even the numerical performance of implicit method is slightly better than explicit method. Reasonable predictions can be derived by explicit method (and implicit method) if the stiffness parameter K_s is selected carefully. As the mapping method does not need to choose Lagrange multiple K_s , this numerical issue can be avoided simultaneously.

Appendix B. Analytical solution for pin-pin beam

In this Appendix, we briefly review the analytical solution for dynamics of a pin-pin beam. The classical Euler–Bernoulli beam theory assumes the structural deflection $w(x, t)$ is only a function of x coordinate (with $x \in [0, L]$) rather than its arclength $s(x, y)$, and the bending curvature is assumed to be, $\kappa \approx \partial^2 w / \partial x^2$. Also, the curvature is only a function of x coordinate, instead of its arclength $s(x, y)$. Overall, the dynamic governing equation of Euler–Bernoulli beam theory is given by

$$EI \frac{\partial^4 w}{\partial x^4} + \rho A \frac{\partial^2 w}{\partial t^2} = 0. \quad (\text{B.1})$$

For a pin-pin beam, $w(x, t)$ has to satisfy the following boundary conditions

$$w|_{x=0} = 0, \quad (\text{B.2a})$$

$$w|_{x=L} = 0, \quad (\text{B.2b})$$

$$EI \frac{\partial^2 w}{\partial x^2} \Big|_{x=0} = 0, \quad (\text{B.2c})$$

$$EI \frac{\partial^2 w}{\partial x^2} \Big|_{x=L} = 0, \quad (\text{B.2d})$$

such that the solution can be written as

$$w(x, t) = \sin(\omega_m t) \sin\left(\frac{m\pi x}{L}\right), \quad (\text{B.3})$$

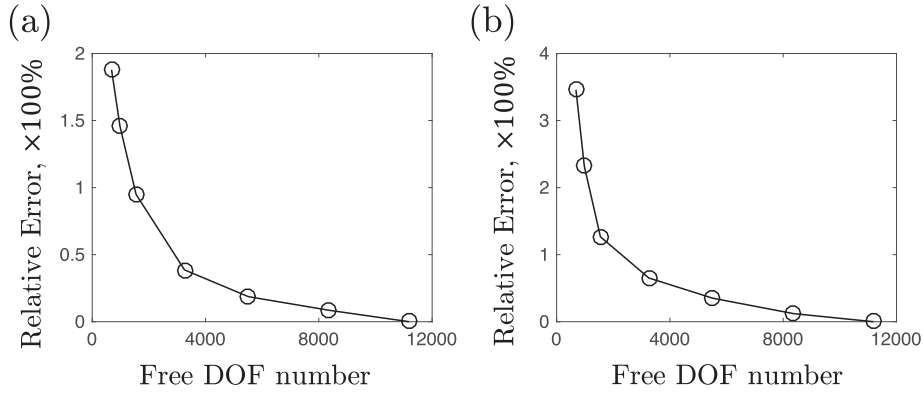


Fig. D1. Convergent study for a gridshell with $n = 14$ rods. (a) Undeformed configuration and (b) Hemispherical shape.

where ω_m is the m th natural frequency and can be evaluated by inserting Eq. (B.3) into Eq. (B.1),

$$\omega_m = \frac{m^2 \pi^2}{L^2} \sqrt{\frac{EI}{\rho A}}. \quad (\text{B.4})$$

Appendix C. Natural frequency of pin-pin beam under compressive load

In this appendix, we derive the analytical solution for a beam with pin-pin boundary conditions under uniaxial compressive load. The dynamic governing equation for Euler–Bernoulli beam under compressive load is

$$EI \frac{\partial^4 w}{\partial x^4} + F \frac{\partial^2 w}{\partial x^2} + \rho A \frac{\partial^2 w}{\partial t^2} = 0, \quad (\text{C.1})$$

and the associated boundary conditions for a PP beam are

$$w|_{x=0} = 0, \quad (\text{C.2a})$$

$$w|_{x=L} = 0, \quad (\text{C.2b})$$

$$EI \frac{\partial^2 w}{\partial x^2} \Big|_{x=0} = 0, \quad (\text{C.2c})$$

$$EI \frac{\partial^2 w}{\partial x^2} \Big|_{x=L} = 0, \quad (\text{C.2d})$$

and, therefore, its solution can be written as

$$w(x, t) = \sin(\omega_m t) \sin\left(\frac{m\pi x}{L}\right), \quad (\text{C.3})$$

where ω_m is the m th natural frequency,

$$\omega_m = \sqrt{\frac{EI m^4 \pi^4 - F m^2 \pi^2 L^2}{\rho A L^4}}. \quad (\text{C.4})$$

When $El\pi^4 - F\pi^2L^2 < 0$, the 1st mode would be negative and meaningless.

Appendix D. Convergent study

In this appendix, a convergent study is performed to show the correctness and accuracy of our numerical model. Here, a gridshell with $n = 14$ rods is considered for demonstration. In Fig. D.17, we plot the relative error as a function of total free DOF number, for (a) undeformed configuration (the one shown in Fig. 10(a1)) and (b) hemispherical shape (the one shown in Fig. 10(a4)). The error is computed as

$$\text{Error} = \frac{|\tilde{\omega}_1 - \tilde{\omega}_{1,\text{true}}|}{|\tilde{\omega}_{1,\text{true}}|}, \quad (\text{D.1})$$

where $\tilde{\omega}_{1,\text{true}}$ is computed when free DOF number is extremely large, e.g., 11187 in this scenario. The error would decrease as the enlargement of DOF number. Notice that the free DOF is approximate 3200 when the size of gridshell is $L = 1\text{m}$ and the discrete edge length is $\Delta l = 1\text{cm}$ (for $n = 14$ rods), which is the discretization used in the current study. The numerical error would be less than 1%.

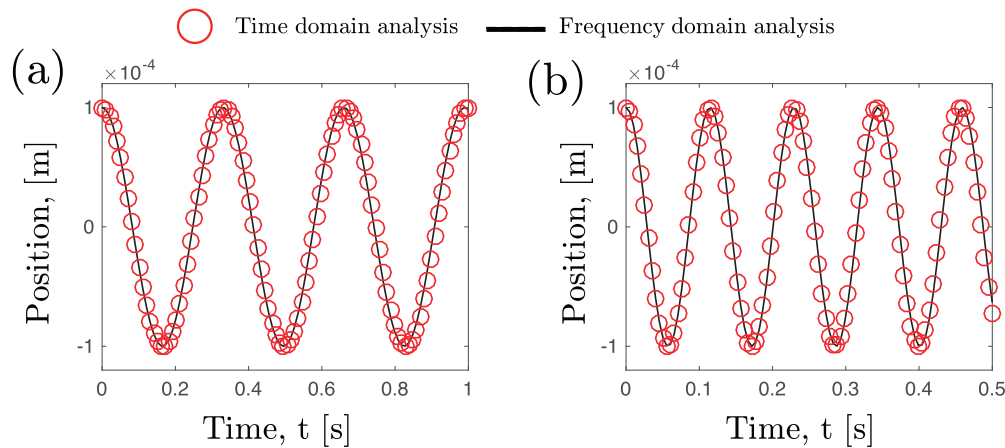


Fig. E1. Position as a function of time for gridshell with (a) $n = 14$ and $\bar{\epsilon} = 0.0$ and (b) $n = 14$ and $\bar{\epsilon} = 1.0$. The line is from frequency domain analysis and the marker is from time integration.

Appendix E. Comparison between time domain analysis and frequency domain analysis

In this appendix, we perform a comparison between time domain analysis and frequency domain analysis. Similar to the previous convergent study, a gridshell with $n = 14$ rods is considered for demonstration. In Fig. E.18(a), we plot the z -position of gridshell midpoint (blue dot in Fig. 10(a1)) as a function of time, for $n = 14$ and $\bar{\epsilon} = 0.0$; next, In Fig. E.18(b), we plot the x -position of gridshell 1/4 point (red dot in Fig. 10(a4)) as a function of time, for $n = 14$ and $\bar{\epsilon} = 1.0$. The frequency domain analysis is derived by checking the eigenvalues and the eigenvectors of associated mass and stiffness matrix, referring to Eq. (18). The time domain analysis is obtained by solving Eq. (16), where the time step size is $h = 1\text{ms}$ and integration parameter is $\beta = 0.5$. Here, the initial condition for time domain analysis is based on the eigenvectors,

$$\tilde{\mathbf{q}}_{\text{initial}} = \tilde{\mathbf{q}}_{\text{equilibrium}} + A_m \delta \tilde{\mathbf{q}}_1, \quad (\text{E.1})$$

where $\delta \tilde{\mathbf{q}}_1$ is the 1st eigenvector and A_m is the vibration magnitude and is chosen to be 10^{-4} for the reference points, e.g., Fig. E.18(a) is for the blue dot shown in Figs. 10(a1) and E.18(b) is for the red dot shown in Fig. 10(a4). With this initial condition, the structure would vibrate as first natural frequency. Quantitative agreements have been found between time domain analysis and frequency domain analysis.

Supplementary material

Supplementary material associated with this article can be found, in the online version, at doi:10.1016/j.apm.2022.03.011.

References

- [1] C. Lestringant, B. Audoly, D.M. Kochmann, A discrete, geometrically exact method for simulating nonlinear, elastic and inelastic beams, *Comput. Methods Appl. Mech. Eng.* (2019) 112741.
- [2] W. Huang, Y. Wang, X. Li, M.K. Jawed, Shear induced supercritical pitchfork bifurcation of pre-buckled bands, from narrow strips to wide plates, *J. Mech. Phys. Solids* 145 (2020) 104168.
- [3] M. Ghiyasinasab, N. Lehoux, S. Ménard, Production phases and market for timber gridshell structures: a state-of-the-art review, *BioResources* 12 (4) (2017) 9538–9555.
- [4] J.A. Fan, W.-H. Yeo, Y. Su, Y. Hattori, W. Lee, S.-Y. Jung, Y. Zhang, Z. Liu, H. Cheng, L. Falgout, Fractal design concepts for stretchable electronics, *Nat. Commun.* 5 (2014) 3266.
- [5] K.-I. Jang, K. Li, H.U. Chung, S. Xu, H.N. Jung, Y. Yang, J.W. Kwak, H.H. Jung, J. Song, C. Yang, Self-assembled three dimensional network designs for soft electronics, *Nat. Commun.* 8 (2017) 15894.
- [6] Y. Li, J. Song, B. Fang, J. Zhang, Surface effects on the postbuckling of nanowires, *J. Phys. D* 44 (42) (2011) 425304.
- [7] S. Xu, Z. Yan, K.-I. Jang, W. Huang, H. Fu, J. Kim, Z. Wei, M. Flavin, J. McCracken, R. Wang, Assembly of micro/nanomaterials into complex, three-dimensional architectures by compressive buckling, *Science* 347 (6218) (2015) 154–159.
- [8] H. Zhao, K. Li, M. Han, F. Zhu, A. Vázquez-Guardado, P. Guo, Z. Xie, Y. Park, L. Chen, X. Wang, Buckling and twisting of advanced materials into morphable 3D mesostructures, *Proc. Natl. Acad. Sci.* (2019) 201901193.
- [9] K.-I. Jang, H.U. Chung, S. Xu, C.H. Lee, H. Luan, J. Jeong, H. Cheng, G.-T. Kim, S.Y. Han, J.W. Lee, Soft network composite materials with deterministic and bio-inspired designs, *Nat. Commun.* 6 (2015) 6566.
- [10] Z. Xu, Z. Fan, H. Fu, Y. Liu, Y. Zi, Y. Huang, Y. Zhang, Optimization-based approach for the inverse design of ribbon-shaped three-dimensional structures assembled through compressive buckling, *Phys. Rev. Appl.* 11 (5) (2019) 054053.
- [11] P.M. Reis, F.L. Jiménez, J. Marthelot, Transforming architectures inspired by origami, *Proc. Natl. Acad. Sci.* 112 (40) (2015) 12234–12235.
- [12] E.T. Filipov, T. Tachi, G.H. Paulino, Origami tubes assembled into stiff, yet reconfigurable structures and metamaterials, *Proc. Natl. Acad. Sci.* 112 (40) (2015) 12321–12326.
- [13] B. Audoly, Y. Pomeau, *Elasticity and Geometry: From Hair Curls to the Non-linear Response of Shells*, Oxford University Press, 2010.
- [14] M.K. Jawed, A. Novelia, O.M. O'Reilly, *A Primer on the Kinematics of Discrete Elastic Rods*, Springer, 2018.

- [15] S.S. Antman, C.S. Kenney, Large buckled states of nonlinearly elastic rods under torsion, thrust, and gravity, *Arch. Ration. Mech. Anal.* 76 (4) (1981) 289–338.
- [16] S.S. Antman, K.B. Jordan, 5.—Qualitative aspects of the spatial deformation of non-linearly elastic rods, *Proc. R. Soc. Edinb. Sect. A* 73 (1975) 85–105.
- [17] S. Kehrbaum, J.H. Maddocks, Elastic rods, rigid bodies, quaternions and the last quadrature, in: *Localization And Solitary Waves In Solid Mechanics*, World Scientific, 1999, pp. 181–200.
- [18] M. Nizette, A. Goriely, Towards a classification of Euler–Kirchhoff filaments, *J. Math. Phys.* 40 (6) (1999) 2830–2866.
- [19] O. Ameline, S. Haliyo, X. Huang, J.A.H. Cognet, Classifications of ideal 3D elastica shapes at equilibrium, *J. Math. Phys.* 58 (6) (2017) 062902.
- [20] T. Yu, L. Dreier, F. Marmo, S. Gabriele, S. Parascho, S. Adriaenssens, Numerical modeling of static equilibria and bifurcations in bigons and bigon rings, *J. Mech. Phys. Solids* 152 (2021) 104459.
- [21] M. Bergou, B. Audoly, E. Vouga, M. Wardetzky, E. Grinspun, Discrete viscous threads, in: *ACM Transactions on Graphics (TOG)*, vol. 29, ACM, 2010, p. 116.
- [22] M. Batista, Large deflection of cantilever rod pulled by cable, *Appl. Math. Model.* 39 (10–11) (2015) 3175–3182.
- [23] Y. Wang, F.-M. Li, Nonlinear dynamics modeling and analysis of two rods connected by a joint with clearance, *Appl. Math. Model.* 39 (9) (2015) 2518–2527.
- [24] S.V. Levyakov, Formulation of a geometrically nonlinear 3D beam finite element based on kinematic-group approach, *Appl. Math. Model.* 39 (20) (2015) 6207–6222.
- [25] W. Huang, X. Huang, C. Majidi, M.K. Jawed, Dynamic simulation of articulated soft robots, *Nat. Commun.* 11 (1) (2020) 1–9.
- [26] B. Audoly, N. Clauvelin, P.-T. Brun, M. Bergou, E. Grinspun, M. Wardetzky, A discrete geometric approach for simulating the dynamics of thin viscous threads, *J. Comput. Phys.* 253 (2013) 18–49.
- [27] Z. Shen, J. Huang, W. Chen, H. Bao, Geometrically exact simulation of inextensible ribbon, in: *Computer Graphics Forum*, vol. 34, Wiley Online Library, 2015, pp. 145–154.
- [28] R. Charrondière, F. Bertails-Descoubes, S. Neukirch, V. Romero, Numerical modeling of inextensible elastic ribbons with curvature-based elements, *Comput. Methods Appl. Mech. Eng.* 364 (2020) 112922.
- [29] W. Huang, C. Ma, L. Qin, Snap-through behaviors of a pre-deformed ribbon under midpoint loadings, *Int. J. Solids Struct.* 232 (2021) 111184.
- [30] D. Baraff, A. Witkin, Large steps in cloth simulation, in: *Proceedings of the 25th Annual Conference on Computer Graphics and Interactive Techniques*, ACM, 1998, pp. 43–54.
- [31] E. Grinspun, P. Krysl, P. Schröder, Chams: a simple framework for adaptive simulation, in: *ACM Transactions on Graphics (TOG)*, vol. 21, ACM, 2002, pp. 281–290.
- [32] E. Grinspun, A.N. Hirani, M. Desbrun, P. Schröder, Discrete shells, in: *Proceedings of the 2003 ACM SIGGRAPH/Eurographics Symposium on Computer Animation*, Eurographics Association, 2003, pp. 62–67.
- [33] E. Ruocco, J.N. Reddy, A discrete differential geometry-based approach to buckling and vibration analyses of inhomogeneous Reddy plates, *Appl. Math. Model.* 100 (2021) 342–364.
- [34] C. Baek, A.O. Sageman-Furnas, M.K. Jawed, P.M. Reis, Form finding in elastic gridshells, *Proc. Natl. Acad. Sci.* 115 (1) (2018) 75–80.
- [35] C. Baek, P.M. Reis, Rigidity of hemispherical elastic gridshells under point load indentation, *J. Mech. Phys. Solids* 124 (2019) 411–426.
- [36] J. Spillmann, M. Teschner, Cosserat nets, *IEEE Trans. Vis. Comput. Graph.* 15 (2) (2008) 325–338.
- [37] J. Pérez, B. Thomaszewski, S. Coros, B. Bickel, J.A. Canabal, R. Sumner, M.A. Otaduy, Design and fabrication of flexible rod meshes, *ACM Trans. Graph. (TOG)* 34 (4) (2015) 138.
- [38] J. Panetta, M. Konaković-Luković, F. Ivoranu, E. Bouleau, M. Pauly, X-shells: a new class of deployable beam structures, *ACM Trans. Graph. (TOG)* 38 (4) (2019) 83.
- [39] W. Huang, L. Qin, M. Khalid Jawed, Numerical method for direct solution to form-finding problem in convex gridshell, *J. Appl. Mech.* 88 (2) (2021).
- [40] W. Huang, L. Qin, Q. Chen, Numerical exploration on snap buckling of a pre-stressed hemispherical gridshell, *J. Appl. Mech.* 89 (1) (2021) 011005.
- [41] L. Qin, W. Huang, Y. Du, L. Zheng, M.K. Jawed, Genetic algorithm-based inverse design of elastic gridshells, *Struct. Multidiscip. Optim.* (2020) 1–17.
- [42] H. Wada, Transient longitudinal vibrations of a finite cylindrical rod connected to an elastic half-space, *J. Sound Vib.* 82 (3) (1982) 383–390.
- [43] N.N. Goldberg, O.M. O'Reilly, On contact point motion in the vibration analysis of elastic rods, *J. Sound Vib.* 487 (2020) 115579.
- [44] Z. Liu, P. Ye, X. Guo, Y. Guo, Rigid-flexible coupling dynamic analysis on a mass attached to a rotating flexible rod, *Appl. Math. Model.* 38 (21–22) (2014) 4985–4994.
- [45] N.N. Goldberg, O.M. O'Reilly, Pervasive nonlinear vibrations due to rod-obstacle contact, *Nonlinear Dyn.* 103 (3) (2021) 2169–2181.
- [46] A.J. Peck, M.Y. Shatalov, S.V. Joubert, Longitudinal vibrations of a lightly damped viscoelastic rod growing in both lateral and axial directions, *Appl. Math. Model.* 101 (2022) 332–352.
- [47] K. Yang, A unified solution for longitudinal wave propagation in an elastic rod, *J. Sound Vib.* 314 (1–2) (2008) 307–329.
- [48] Q.-t. Deng, S.-n. Luo, Characteristics of wave propagation in piezoelectric bent rods with arbitrary curvature, *Appl. Math. Model.* 35 (5) (2011) 2557–2570.
- [49] R.B. Nielsen, S.V. Sorokin, Periodicity effects of axial waves in elastic compound rods, *J. Sound Vib.* 353 (2015) 135–149.
- [50] H. Cetin, G. Yaralioglu, Coriolis effect on elastic waves propagating in rods, *J. Sound Vib.* 485 (2020) 115545.
- [51] H. Wang, X. Ning, H. Li, H. Luan, Y. Xue, X. Yu, Z. Fan, L. Li, J.A. Rogers, Y. Zhang, Vibration of mechanically-assembled 3Dmicrostructures formed by compressive buckling, *J. Mech. Phys. Solids* 112 (2018) 187–208.
- [52] Y. Wang, X. Cui, H. Fu, Q. Zhao, Y. Li, Dynamic behaviors of postbuckled thin film on flexible substrates considering viscoelastic effects, *J. Appl. Mech.* 88 (4) (2021) 041007.
- [53] H. Li, X. Wang, H. Wang, J. Chen, The nonlocal multi-directional vibration behaviors of buckled viscoelastic nanoribbons, *Proc. Inst. Mech. Eng., Part C* 234 (18) (2020) 3571–3583.
- [54] M.L. Regalo, S. Gabriele, G. Salerno, V. Varano, Numerical methods for post-formed timber gridshells: simulation of the forming process and assessment of r-funicularity, *Eng. Struct.* 206 (2020) 110119.
- [55] W. Huang, L. Qin, Q. Chen, Numerical exploration on snap buckling of a pre-stressed hemispherical gridshell, *J. Appl. Mech.* 89 (1) (2022).
- [56] E.J. Doedel, Lecture notes on numerical analysis of nonlinear equations, in: *Numerical Continuation Methods for Dynamical Systems*, Springer, 2007, pp. 1–49.
- [57] B. Audoly, S. Neukirch, A one-dimensional model for elastic ribbons: a little stretching makes a big difference (2021).
- [58] T. Yu, J.A. Hanna, Bifurcations of buckled, clamped anisotropic rods and thin bands under lateral end translations, *J. Mech. Phys. Solids* 122 (2019) 657–685.
- [59] M. Bergou, M. Wardetzky, S. Robinson, B. Audoly, E. Grinspun, Discrete elastic rods, in: *ACM Transactions on Graphics (TOG)*, vol. 27, ACM, 2008, p. 63.
- [60] W. Huang, M.K. Jawed, Newmark-beta method in discrete elastic rods algorithm to avoid energy dissipation, *J. Appl. Mech.* 86 (8) (2019) 084501.